

REGULAR PAPER

SiC quantum dot formation in SiO₂ layer using double hot-Si⁺/C⁺-ion implantation technique

To cite this article: Tomohisa Mizuno *et al* 2020 *Jpn. J. Appl. Phys.* **59** SGGH02

View the [article online](#) for updates and enhancements.



SiC quantum dot formation in SiO₂ layer using double hot-Si⁺/C⁺-ion implantation technique

Tomohisa Mizuno^{1*}, Rikito Kanazawa¹, Takashi Aoki¹, and Toshiyuki Sameshima²¹Department of Science, Kanagawa University, Hiratsuka, Kanagawa 259-1293, Japan²Department of Engineering, Tokyo University of Agriculture and Technology, Koganei, Tokyo 184-8588, Japan*E-mail: mizuno@kanagawa-u.ac.jp

Received September 27, 2019; revised October 25, 2019; accepted November 26, 2019; published online February 6, 2020

We experimentally studied the material structure and photoluminescence (PL) properties of SiC quantum-dots (QD) in SiO₂ layer (Si⁺/C⁺-OX) fabricated by double hot-Si⁺/C⁺ ion implantation into SiO₂ and the post N₂ annealing, comparing with those of SiC-dots by single hot-C⁺ ion implanted oxide (C⁺-OX) and crystal-Si layers (C⁺-Si). X-ray photoemission spectroscopy for Si⁺/C⁺-OX confirmed Si-C bonds even in SiO₂, which is the direct verification of SiC formation in SiO₂. Moreover, transmission electron microscope analyzes showed that 2 nm diameter SiC-dots with a clear lattice spots were successfully formed in Si⁺/C⁺-OX. After N₂ annealing, we demonstrated strong PL emission from Si⁺/C⁺-OX, and the PL intensity I_{PL} of Si⁺/C⁺-OX is approximately 2.6 and 12 times larger than those of C⁺-Si and C⁺-OX, respectively. The stronger I_{PL} of Si⁺/C⁺-OX is possibly attributable to QD-induced PL-efficiency enhancement in Si⁺/C⁺-OX. Moreover, PL photon energy at the peak I_{PL} of Si⁺/C⁺-OX rapidly increases to approximately 2.4 eV after N₂ annealing. © 2020 The Japan Society of Applied Physics

1. Introduction

A Si nano-structure, such as a two-dimensional (2D) Si layer, is widely studied to evaluate the quantum mechanical phenomena as well as to realize both Si-based photonic¹⁻¹⁵ and scaled CMOS devices.¹⁶ The peak photoluminescence (PL) photon wavelength λ_{PL} is longer than 650 nm and the PL intensity I_{PL} is too low for the Si-based visible-photonic devices.^{9,14} Thus, Si-C alloy,¹⁷⁻¹⁹ Si_{1-y}C_y and silicon-carbide (SiC)^{20,21} are candidates for the Si-based visible-photonic devices, because of their large bandgap E_G . 3D-SiC can emit the PL photons by many recombination processes, such as, free exciton recombination,²⁰⁻²² while 3D-SiC has an indirect bandgap structure.^{20,21} As a result, the PL photon energy E_{PH} of 3D-SiC is equal to the exciton energy gap E_{GX} which is approximately 0.1 eV lower than E_G .^{20,21} Moreover, there are many diverse polytypes in SiC whose physical properties including E_G strongly depend on the polytype,^{20,21} and thus it is possible that the λ_{PL} of SiC photonic devices can be controlled by the polytype. Since the E_G of SiC also depends on the size dimension of SiC,²⁰ SiC nanostructures,²⁰ such as a porous-SiC,^{20,23-25} 2D-SiC,^{20,26,27} SiC-nanowire,^{20,28,29} and SiC-dot,^{20,30,31} are also candidates not only for material science including quantum effects, but also for emission wavelength controlled photonic devices.

Recently, to study the material science of SiC nanostructure, as well as to realize a Si-based photonic derives in the wide range of λ_{PL} from visible range to near-UV, we have experimentally studied a several-nm size SiC-dot fabricated by hot-¹²C⁺-ion implantation into a Si substrate at a high substrate temperature T and heavy C⁺ ion dose D_C in the wide range of $500\text{ }^\circ\text{C} \leq T \leq 1000\text{ }^\circ\text{C}$ and $5 \times 10^{12} \leq D_C \leq 7 \times 10^{16}\text{ cm}^{-2}$ ($0.01 < Y \leq 0.3$).^{32,33} X-ray photoelectron spectroscopy (XPS) showed Si-C bond in hot-¹²C⁺-ion implanted Si layer, which is the direct verification of SiC formation in Si layer.³²⁻³⁵ As a result, we confirmed that the PL intensity increases with increasing D_C . The self-cluster effects of ion-implanted C atoms in a crystal-Si (c-Si) layer,^{34,35} analyzed by atom probe tomography,³⁵⁻³⁷ leads to the local condensation of C-atoms with the size of several nm both at the oxide/Si interface and in c-Si layer. This is the physical mechanism for the local

formation of SiC nano-dots in Si areas.³²⁻³⁵ The hot-C⁺-ion implantation process can reduce the ion implantation-induced damage of the Si layer, which is the advantageous characteristics of hot-C⁺-ion implantation process.³³ Moreover, the partial formation of cubic (3C-SiC) and hexagonal SiC (H-SiC) nano-dots were also confirmed both at oxide/Si interface and in the Si layer, using corrector-spherical aberration transmission electron microscopy (CSTEM), high-angle annular-dark-field (HAADF) scanning transmission electron microscope (STEM), and electron diffraction patterns that were obtained by fast Fourier transform analysis of the lattice spots of CSTEM data.^{34,35} We also demonstrated very large E_{PH} (≈ 3 eV) and very strong PL intensities (I_{PL}) from the near-UV to visible regions (>350 nm) of SiC dots, which markedly increase with increasing the C content in Si layer. For example, the PL emission from SiC dots is about 100 times stronger than that from 2D-Si.³³ The optimum T is $400\text{ }^\circ\text{C} - 900\text{ }^\circ\text{C}$ to realize strong PL emission, which is much lower than the usual bulk-SiC formation ($>1300\text{ }^\circ\text{C}$).²¹ This is the characteristic of hot-C⁺-ion implantation process. Moreover, even in an amorphous-Si (a-Si) and poly-Si substrates³⁸ as well as in a bulk-Si substrate,^{39,40} SiC nano-dots were successfully formed and the strong PL emission was observed. Thus, the crystal structure of Si layer is not essential for the SiC dot formation in Si material by hot-C⁺-ion implantation. However, the SiC dot diameter R , surface density N , and PL properties (I_{PL} and E_{PH}) strongly depend on the hot-C⁺-ion implantation process conditions,⁴⁰ the crystal structure of Si^{35,38-40} and the c-Si surface orientation.³⁹ For example, the R and N in hot-C⁺-ion implanted c-Si (C⁺-Si) were approximately 2.9 nm and $1.6 \times 10^{12}\text{ cm}^{-2}$, respectively.⁴⁰

These SiC dots with larger E_G (≥ 2.4 eV) are embedded in Si layer with smaller E_G (≈ 1.1 eV).⁴¹ As a result, the SiC dot in Si layer is not a quantum dot (QD), resulting in too small PL quantum efficiency for visible Si-based photonic devices. Therefore, it is strongly required to realize a SiC-QD embedded in much larger E_G material, such as SiO₂ with $E_G \approx 9$ eV,⁴¹ and thus the PL quantum efficiency of SiC-QD can be improved by band-to-band recombination of excited electrons as well as free exciton recombination. The SiC-QD formation in SiO₂ has been already reported to be studied by

the room-temperature co-implantation process of high-dose Si^+ and C^+ ions into SiO_2 ,^{20,42)} but the room-temperature high-dose ion implantation creates many defects in SiC-QD, which leads to the PL intensity reduction.⁴²⁾ In addition, the quantum confinement effects of SiC-QD, such as the dot diameter dependence of E_G ,^{20,41)} has not been confirmed.⁴²⁾ Thus, it is strongly required to improve the high-dose ion implantation process, and it is expected that the hot-ion implantation process is very promising for realizing a SiC-QD in Si-oxide.

In this work, we experimentally studied the SiC-QD embedded in SiO_2 , fabricated by double hot- Si^+/C^+ -ion implantation into a SOX layer ($\text{Si}^+/\text{C}^+-\text{OX}$) on bulk-Si and the post N_2 annealing.⁴³⁾ Si-C bond even in the SiO_2 of $\text{Si}^+/\text{C}^+-\text{OX}$ was confirmed by C1s spectrum of XPS, and approximately 2 nm diameter SiC-QDs with clear lattice spots were successfully observed by HAADF-STEM and CSTEM. In addition, we successfully demonstrated that the PL intensity I_{PL} of SiC-QD in $\text{Si}^+/\text{C}^+-\text{OX}$ is much stronger than those of single hot- C^+ -ion implanted oxide (C^+-OX) and bulk-Si layers (C^+-Si), which is possibly the QD effect on the PL coefficient enhancement.

2. Experiment procedure

To fabricate SiC dots in SiO_2 layer, free Si atoms except Si ones bound to O atoms as well as C atoms are required to coexist in SiO_2 , because it is possible that the Si-O bond energy of SiO_2 is too high (the melting point of SiO_2 is 1600 °C)⁴¹⁾ to dissociate the Si-O bond of SiO_2 . Thus, the double hot-ion implantations of Si^+ and the following C^+ ion into the surface SiO_2 (SOX) is the key process to fabricate the SiC-QD in SiO_2 layer, as well as to suppress the defect creation in SiC-dots by high-temperature ion implantation process,³³⁾ as shown in Fig. 1. After forming 150 nm thick SOX [Fig. 1(a)] on (100)bulk-Si substrate, using a usual thermal dry- O_2 oxidation process of a bulk-Si at 1000 °C which is widely used for ULSI processes, hot- Si^+ ions [Fig. 1(b)] and the following hot- C^+ ions [Fig. 1(c)] were implanted into the SOX layer at substrate temperature T (400 °C $\leq T \leq$ 900 °C in this study). A post N_2 annealing was carried out [Fig. 1(d)] at annealing temperature $T_N = 1000$ °C for various annealing time t_N (0 $\leq t_N \leq$ 60 min), to recover the defects of SiC-dots. In addition, as a reference, SiC dots in c-Si were also fabricated by the single hot- C^+ -ion implantation into (100) bulk-Si layer (C^+-Si).⁴⁰⁾ Our previous paper showed that the optimum T

and D_C conditions for C^+-Si were 600 °C and $4 \times 10^{16} \text{ cm}^{-2}$, respectively,⁴⁰⁾ to improve PL intensity. Therefore, the hot-ion implantation conditions of T and ion-dose conditions for Si^+ - (D_S) and C^+ -ion doses (D_C) for $\text{Si}^+/\text{C}^+-\text{OX}$ are determined with reference to the optimum process conditions of C^+-Si ,⁴⁰⁾ as shown in Table I. In addition, to evaluate the effects of the double hot-ion implantations of Si^+ and C^+ on the SiC dot formation in SOX and the PL properties, single hot- C^+ ion (C^+-OX) and single hot- Si^+ (Si^+-OX) implantations into SOX were also carried out, as shown in Fig. 2 which is the same fabrication steps in Fig. 1 except double hot-ion implantation steps. Therefore, the same hot-ion implantation conditions for $\text{Si}^+/\text{C}^+-\text{OX}$ were also used for C^+-OX and Si^+-OX , as shown in Table I, and we also compare the PL properties of $\text{Si}^+/\text{C}^+-\text{OX}$ with those of C^+-OX and Si^+-OX at the same process conditions.

The material structures of the SiC dots were evaluated by HAADF-STEM and CSTEM. Moreover, the C content Y depth profile was evaluated by XPS, whose accuracy was ± 1 at%.⁴⁰⁾ Raman and PL properties were measured at room temperature, where the excitation He-Cd laser energy E_{EX} was 3.8 eV (wavelength = 325 nm), the laser power was approximately 0.6 mW, and the laser diameter was 1 μm . The absorption coefficient of photons at $E_{\text{EX}} = 3.8$ eV is very small in SiO_2 , because E_{EX} is much smaller than the E_G of SiO_2 (≈ 9 eV).⁴¹⁾ As a result, the Raman and PL photons of $\text{Si}^+/\text{C}^+-\text{OX}$, C^+-OX , and Si^+-OX can be detected from all SiC-dots in the whole range of 150 nm SiO_2 , assuming that the overlap effect of SiC-dots of an incident laser can be neglected. However, the Raman and PL photons of C^+-Si are mainly emitted from the SiC nano-dots near the SOX/Si interface, because the photon penetration length λ_{EX} of 3.8 eV laser in Si layer is only 8 nm.^{33,41)} The PL spectrum in the wide range of photon wavelengths λ_{PL} from the UV to

Table I. Hot-ion implantation temperature and ion-dose conditions for four structures of $\text{Si}^+/\text{C}^+-\text{OX}$, C^+-OX , Si^+-OX , and C^+-Si .

Structures	D_S ($\times 10^{16} \text{ cm}^{-2}$)	D_C ($\times 10^{16} \text{ cm}^{-2}$)	T (°C)
$\text{Si}^+/\text{C}^+-\text{OX}$	6	4	400
			600
			900
	10	6	600
C^+-OX		4	600
Si^+-OX	6		
C^+-Si		4	

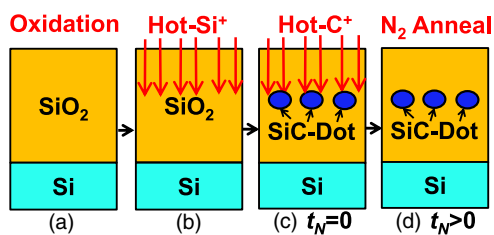


Fig. 1. (Color online) Fabrication steps for $\text{Si}^+/\text{C}^+-\text{OX}$ by double hot- Si^+/C^+ -ion implantation into SOX. After (a) thermal dry- O_2 oxidation process for 150 nm thick SiO_2 on (100) bulk-Si substrate, (b) hot- Si^+ -ions and (c) the following hot- C^+ -ions were implanted into the SOX layer, where hot-ion temperature and ion-dose conditions for $\text{Si}^+/\text{C}^+-\text{OX}$ are shown in Table I. (d) Post N_2 annealing was carried out at $T_N = 1000$ °C for annealing time t_N .

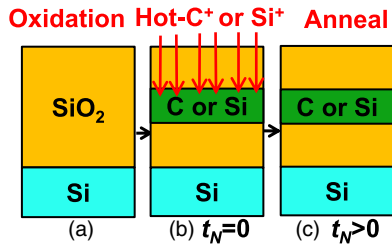


Fig. 2. (Color online) Fabrication steps for C⁺-OX or Si⁺-OX by (b) single hot-C⁺-ion implantation into SOX (C⁺-OX) or single hot-Si⁺-ion implantation into SOX (Si⁺-OX), after (a) thermal dry-O₂ oxidation process of 150 nm thick SiO₂ on (100) bulk-Si substrate. (c) Post N₂ annealing was carried out at T_N = 1000 °C for annealing time t_N.

NIR region was calibrated using a standard illuminant.³³⁾ Moreover, the PL intensity variation within about 1 cm² area of measured sample under each process condition was approximately ±10%. On the other hand, the accuracy of the PL photon energy E_{PH} at the peak PL intensity, obtained by fitting the measured PL spectrum, was estimated to be approximately ±0.04 eV, because of the broad PL spectrum.

3. Results and discussions

3.1. Material structures of Si⁺/C⁺-OX

Firstly, we discuss Si-C bond properties evaluated by XPS analyzes for Si⁺/C⁺-OX.

Figures 3(a) and 3(b) show the C1s and Si2p spectra of Si⁺/C⁺-OX at 84 nm depth (d_{OX}) of the maximum C-dopant density from the SOX surface, respectively, where T = 600 °C, D_S = 6 × 10¹⁶ cm⁻², D_C = 4 × 10¹⁶ cm⁻², and t_N = 30 min. We confirmed the Si-C bond shown as the dashed line in Fig. 3(a), which is the direct verification of SiC formation even in SiO₂. 80% of C atoms bind to Si atoms, and the C content of Si-C bond; Y_C was approximately 4.1 at%. However, 20% of C atoms is separated out in SiO₂, as shown as the dotted line of C-C bond. On the other hand, dotted/dashed, dashed, and dotted lines in Fig. 3(b) show the fitting curves of SiO₂, SiO_x, and SiC_y, respectively. 9% of Si atoms bind to C atoms, and the Si content of Si-C bond; Y_S was approximately 3.3 at%. However, Si-Si bond was not observed, which indicates that implanted Si atoms are not separated out in SiO₂. In summary, we experimentally verified that Y_C ≈ Y_S within the error range of XPS accuracy (1 at%), which indicates that SiC-dots are composed of silicon-carbide not silicon-carbon alloy. On the other hand, the content of O atom in SiO₂, obtained by O1s spectrum, was 58 at% at d_{OX} = 84 nm. In addition, Fig. 3(c) shows the C-content depth profiles of Si-C (solid line) and C-C bonds (dotted line) in SOX evaluated by C1s of Fig. 3(a). The C-content has the maximum value of 4.3 at% at d_{OX} ≈ 84 nm, and the FWHM of C-content is approximately 60 nm. As a result, C ions are not implanted into a Si substrate beneath the SOX layer, and thus SiC-dots are not formed in Si substrate.

Here, the C volume concentration N_C of Si-C bond in the SOX and Si layers can be determined by the volume concentrations of standard atom; N_{ST} in each material. The standard atoms in SiO₂ (Si⁺/C⁺-OX) and in Si layers (C⁺-Si) are O atom (N_{ST} = 4.5 × 10²² cm⁻³)⁴⁴⁾ and Si atom (N_{ST} = 5 × 10²² cm⁻³)⁴¹⁾ respectively, and the concentration variation is estimated by the XPS accuracy of 1 at%. Namely, C volume concentration N(Y) at the content Y (at%) of Si-C

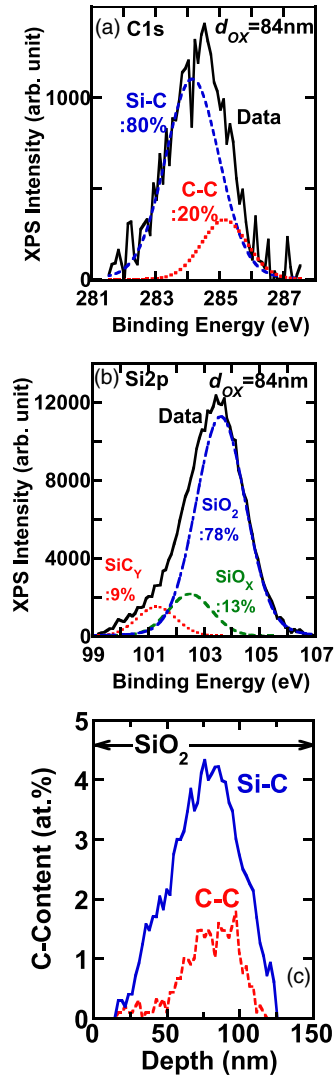


Fig. 3. (Color online) XPS spectra (solid lines) of (a) C1s and (b) Si2p at the depth from the oxide surface; d_{OX} = 84 nm (maximum C-content point), and (c) C-content depth profiles of Si-C (solid line) and C-C bonds (dashed line) in SOX evaluated by C1s, where T = 600 °C, D_S = 6 × 10¹⁶ cm⁻², D_C = 4 × 10¹⁶ cm⁻², and t_N = 30 min. Dashed and dotted lines in (a) show the fitting curves of Si-C and C-C bonds, respectively, which indicates that 80% of C atoms binds to Si atoms and 20% of C atoms is separated out in an oxide layer. Dotted/dashed, dashed, and dotted lines in Fig. 3(b) show the fitting curves of SiO₂, SiO_x, and SiC_y, respectively. Thus, no peak of Si-Si bond indicates that Si atoms are not separated out in an oxide layer. Figure 3(c) shows that the C-contents of Si-C and C-C bonds have the maximum values of approximately 4.3 and 1.5 at% at d_{OX} ≈ 84 nm, respectively, and C-ion dopant area is 20 ≤ d_{OX} ≤ 120 nm.

bond can be given by the following equation

$$N(Y) = \frac{Y}{Y_{ST}} N_{ST}, \quad (1)$$

where Y_{ST} is standard content.

Here, using Eq. (1), Fig. 4 shows the N_C depth profiles of Si-C (solid line) and C-C (dashed line) bonds for Si⁺/C⁺-OX compared with the N_C of Si-C bond for C⁺-Si (dotted line)⁴⁰⁾ at the same conditions of T = 600 °C and D_C = 4 × 10¹⁶ cm⁻² after N₂ annealing, where the lateral origins of Si⁺/C⁺-OX and C⁺-Si are the surface SOX and Si layers, respectively. The C concentration profile of Si-C for Si⁺/C⁺-OX is much different from that for C⁺-Si, and shows very broad and no segregation effects at the surface

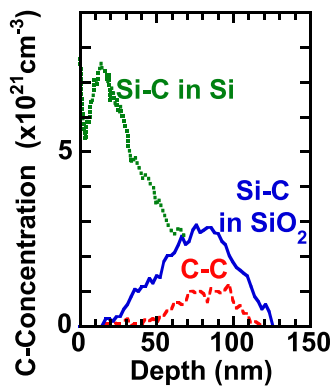


Fig. 4. (Color online) C volume concentrations of Si-C (solid lines) and C-C bonds (dashed line) in SiO₂ (Si⁺/C⁺-OX) at $D_S = 6 \times 10^{16} \text{ cm}^{-2}$ and $t_N = 30 \text{ min}$, and C volume concentration of Si-C band (dotted line) in c-Si layers (C⁺-Si) at $t_N = 5 \text{ min}$ estimated by Eq. (1) and XPS data at the same D_C , where $D_C = 4 \times 10^{16} \text{ cm}^{-2}$, $T = 600 \text{ }^\circ\text{C}$, and $T_N = 1000 \text{ }^\circ\text{C}$. The origins of the lateral axis for Si⁺/C⁺-OX and C⁺-Si are the SiO₂-surface and Si-surface, respectively. The peak C concentrations in SiO₂ and Si layers are estimated to 2.8×10^{21} and $7.5 \times 10^{21} \text{ cm}^{-3}$, respectively. Even at the same D_C , the C concentration of Si-C bond in C⁺-Si is approximately 2.5 times higher than that in Si⁺/C⁺-OX, whereas the C-C bond disappears in Si layer of C⁺-Si.

SOX. The maximum N_C value of Si⁺/C⁺-OX ($\approx 2.8 \times 10^{21} \text{ cm}^{-3}$) is approximately 37% of that of C⁺-Si ($\approx 7.3 \times 10^{21} \text{ cm}^{-3}$). Thus, even at the same conditions of hot-C⁺ ion implantation, it is expected that the SiC dot formation between Si⁺/C⁺-OX and C⁺-Si is much different. On the other hand, the C-C bond in C⁺-Si was not observed, which indicates that implanted C atom separation occurs only in a SiO₂ except Si layer.

Next, we discuss the SiC-dot structure evaluated by HAADF-STEM analysis. Since SiC dots in SOX are local Si-rich areas, HAADF-STEM image for Si⁺/C⁺-OX shows that SiC dot areas indicate bright dots, as shown in Figs. 5(b)–5(c). Figures 5(a) and 5(b) show HAADF-STEM images of the cross section of surface Si⁺/C⁺-OX at low T of 400 °C before ($t_N = 0$) and after N₂ annealing ($t_N = 30 \text{ min}$), respectively, where $D_S = 6 \times 10^{16} \text{ cm}^{-2}$ and $D_C = 4 \times 10^{16} \text{ cm}^{-2}$. Before N₂ annealing, Fig. 5(a) shows that clear SiC-dots are not observed, which suggests that SiC-dot formation is rare. However, after N₂ annealing, Fig. 5(b) shows that many bright dots, that is, SiC dots are successfully formed below approximately 20 nm depth from the surface SOX, whose region is the C-rich area of the C content of Si-C band of higher than 0.5 at%, as shown in Fig. 3(c). Thus, the post N₂ annealing is also the key process to form SiC-dots in SOX. Moreover, Fig. 5(c) also show the HAADF-STEM image of the cross section of surface Si⁺/C⁺-OX at high T of 600 °C at $t_N = 30 \text{ min}$, where $D_S = 6 \times 10^{16} \text{ cm}^{-2}$ and $D_C = 4 \times 10^{16} \text{ cm}^{-2}$, and indicates that many SiC-dots are also formed at $T = 600 \text{ }^\circ\text{C}$. Figures 5(b) and 5(c) show that average SiC-dot diameter R and SiC-dot surface density N depend on T . As shown in Fig. 5(d), the R of low and high T are estimated to be approximately 2 and 4 nm, respectively, and the N of low and high T are approximately 1.4×10^{12} and $5 \times 10^{11} \text{ cm}^{-2}$, respectively. Namely, with decreasing T , average R decreases, but the N increases, which is the same tendency of the R and N of C⁺-Si.⁴⁰ On the other hand, at the same process conditions of $T = 600 \text{ }^\circ\text{C}$ and $D_C = 4 \times 10^{16} \text{ cm}^{-2}$ after N₂ annealing, the R and N of C⁺-Si were 3 nm and $4 \times 10^{12} \text{ cm}^{-2}$,

respectively, and thus, the R of Si⁺/C⁺-OX is approximately 1.3 times as large as that of C⁺-Si. On the other hand, the N of Si⁺/C⁺-OX are only 13% of that of C⁺-Si, because of lower C-concentration of Si⁺/C⁺-OX, as shown in Fig. 4.

Moreover, Figs. 6(a) and 6(b) show the lattice images evaluated by CSTEM of the cross section of SiC-dots in SiO₂ of Si⁺/C⁺-OX, as the same process conditions of Fig. 5(b), and clear lattice spots of SiC-dots encircled can be observed even in SiO₂ of Si⁺/C⁺-OX. These linear lattice spots without hexagonal structures suggest that the polytype of SiC-dots in Si⁺/C⁺-OX is 3C-SiC with the E_G of 2.4 eV,^{20,21} which is already identified in SiC-dots of C⁺-Si.^{33,35,38,40} The diameters of SiC-dots in Figs. 6(a) and 6(b) are 1.6 and 2.2 nm, respectively, which is almost the same as the HAADF-STEM results in Fig. 5(b).

3.2. UV-Raman properties

In this Sect. 3.2, we discuss the material structures of SiC-dots evaluated by UV-Raman spectroscopy.

Figure 7 shows the UV-Raman spectra of Si⁺/C⁺-OX (solid line) at $D_S = 6 \times 10^{16} \text{ cm}^{-2}$ and C⁺-Si (dotted line), where $T = 600 \text{ }^\circ\text{C}$, $D_C = 4 \times 10^{16} \text{ cm}^{-2}$, and $t_N = 0$. It is noted that UV-Raman analysis of Si⁺/C⁺-OX shows the strong two peaks of the T-band around 1100 cm^{-1} originated from C-C sp^3 vibrations of a-C^{45–47} and D-band of C-C sp^2 vibrations without G-band peak, which suggests that a-C in Si⁺/C⁺-OX mainly consists of diamond-like carbon (sp^3 site).^{45,47} However, the TO-mode intensity (I_{TO}) of Si-C vibration^{20,21} is very weak, compared with those of T-band (I_T) and D-band (I_D), which is the characteristic of SiC-dots.²⁰ In addition, the LO-mode peak around 960 cm^{-1} was not observed even in C⁺-Si, because the LO-mode rapidly decreases in SiC-dots.²⁰ On the other hand, C⁺-Si shows TO, D, and G-bands, but the peak of T-band was not observed, which indicates that a-C formation is very rare in C⁺-Si. The Raman intensity of Si⁺/C⁺-OX is almost the same as that of C⁺-Si. Since the Raman intensity ratio of D-band to G-band⁴⁵ was 0.54 in C⁺-Si, the defect density of C-material in C⁺-Si is much smaller than that in Si⁺/C⁺-OX. Consequently, the TO-mode shown in Fig. 7 shows that Si-C vibration is also verified in both Si⁺/C⁺-OX and C⁺-Si.

Next, Figs. 8(a) and 8(b) show the T dependence of UV-Raman spectrum and peak Raman intensities of TO-mode (triangles), T-band (squares), and D-band (circles) for Si⁺/C⁺-OX, where $D_S = 6 \times 10^{16} \text{ cm}^{-2}$, $D_C = 4 \times 10^{16} \text{ cm}^{-2}$, and $t_N = 0$. Figure 8(a) shows that the Raman spectrum line shape is almost independent of T , and the Raman properties are independent of T at $400 \text{ }^\circ\text{C} \leq T \leq 600 \text{ }^\circ\text{C}$. However, the Raman intensity I_R rapidly decreases at $T = 900 \text{ }^\circ\text{C}$. This T dependence of each peak I_R is very clear in Fig. 8(b), and all I_R keep constant at $T \leq 600 \text{ }^\circ\text{C}$, but rapidly decreases at $T = 900 \text{ }^\circ\text{C}$. The rapid I_R reduction at $T = 900 \text{ }^\circ\text{C}$ is possibly attributable to the out-diffusion of C atoms from SOX layer during high- T (900 °C) hot-ion implantation process.

On the other hand, Figs. 9(a) and 9(b) show the post N₂ annealing time t_N dependence of the peak- I_R of I_{TO} (triangles), I_T (squares), and I_D (circles), and the peak Raman position shift of TO-mode, T-band, and D-band for Si⁺/C⁺-OX, respectively, where $T = 600 \text{ }^\circ\text{C}$, $D_S = 6 \times 10^{16} \text{ cm}^{-2}$, and $D_C = 4 \times 10^{16} \text{ cm}^{-2}$. Figure 9(a) shows that I_{TO} rapidly increases at $t_N \approx 5 \text{ min}$, which is attributable to the rapid

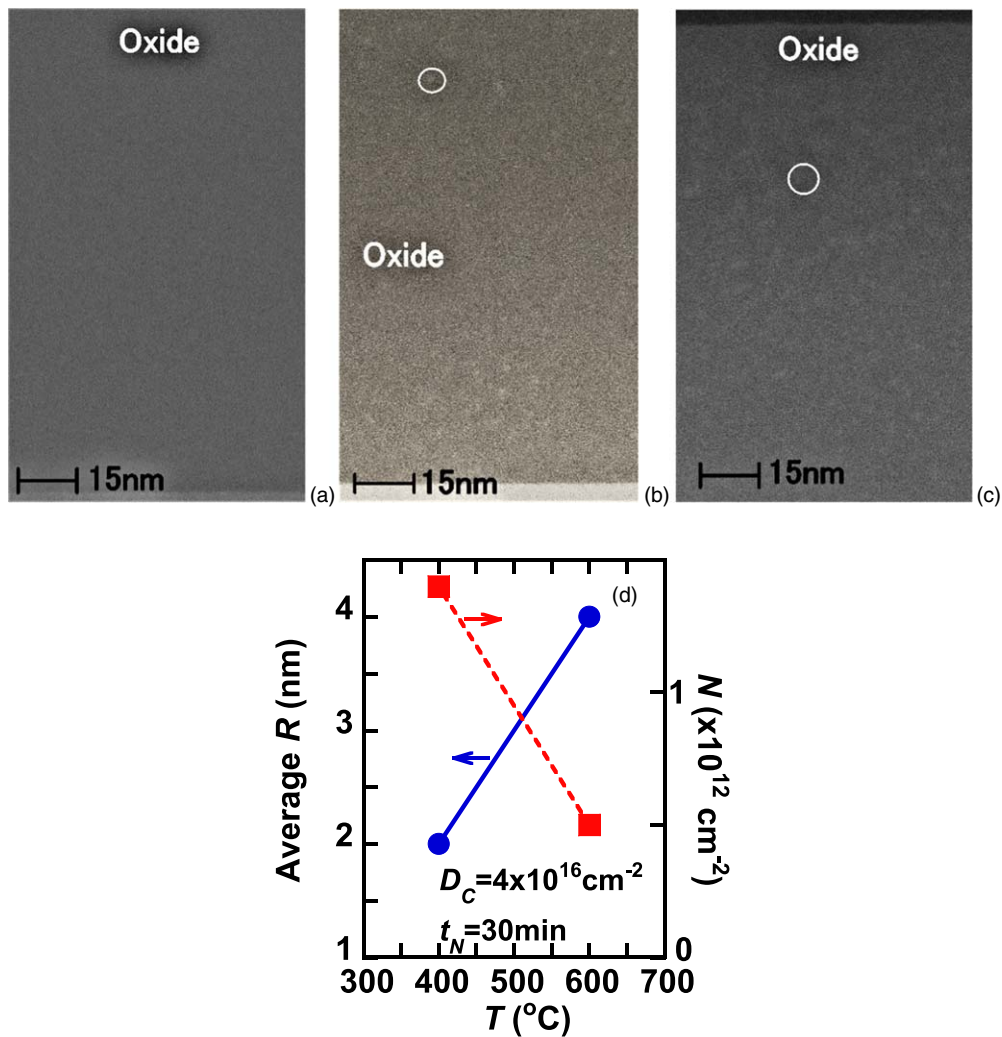


Fig. 5. (Color online) HAADF-STEM images of the cross section of SiC dots (bright areas) encircled in SOX of Si⁺/C⁺-OX (a) at $t_N = 0$ and $T = 400$ °C, (b) at $t_N = 30$ min and $T = 400$ °C, and (c) at $T = 600$ °C and $t_N = 30$ min, where $D_S = 6 \times 10^{16}$ cm⁻² and $D_C = 4 \times 10^{16}$ cm⁻². SiC dots in SOX are the Si rich area, resulting in the bright areas in HAADF-STEM image. Before N₂ annealing, Fig. 5(a) shows that clear SiC-dots cannot be observed. However, after N₂ annealing, Figs. 5(b) and 5(c) show that many SiC dots are verified below 20 nm depth from the SOX surface, but the R and surface density N of SiC-dots depend on T . (d) Average R and N of SiC-dots versus T at the same process conditions of Figs. 5(b) and 5(c), where $t_N = 30$ min. With increasing T , the R increases, and on the contrary the N decreases.

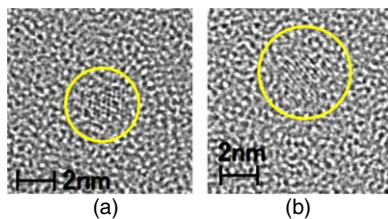


Fig. 6. (Color online) CSTEM images of lattice spots of SiC-dots encircled in SiO₂ layer of Si⁺/C⁺-OX, as the same conditions of Fig. 5(b), where $t_N = 30$ min, $T = 400$ °C, $D_S = 6 \times 10^{16}$ cm⁻² and $D_C = 4 \times 10^{16}$ cm⁻². Clear and linear lattice spots suggest that the polytype of SiC-dots is 3C-SiC. The diameters of SiC-dots in Figs. 6(a) and 6(b) are 1.6 and 2.2 nm, respectively.

SiC-dot formation after N₂ annealing, as shown as the HAADF-STEM observations in Figs. 5(a) and 5(b). Moreover, both I_T and I_D also increase at $t_N \approx 5$ min, which is possibly attributable to the reduction of defects of C material during N₂ annealing at high T_N of 1000 °C. However, all

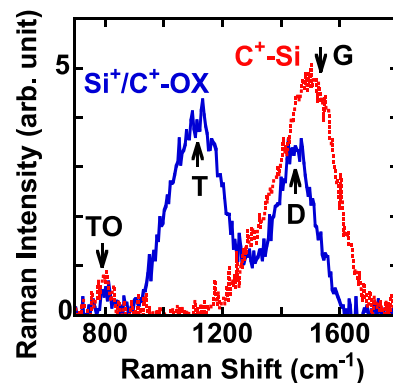


Fig. 7. (Color online) UV-Raman spectra of Si⁺/C⁺-OX (solid line) at $D_S = 6 \times 10^{16}$ cm⁻² and C⁺-Si (dotted line), where $D_C = 4 \times 10^{16}$ cm⁻² and $t_N = 0$. The arrows of Si⁺/C⁺-OX show the strong D and T bands of C-C vibration and weak TO mode of Si-C vibration, and C⁺-Si also shows the strong G and D bands of C-C vibration, and weak TO mode of Si-C vibration. Thus, Si⁺/C⁺-OX shows no G-band, and on the contrary C⁺-Si shows no T-band.

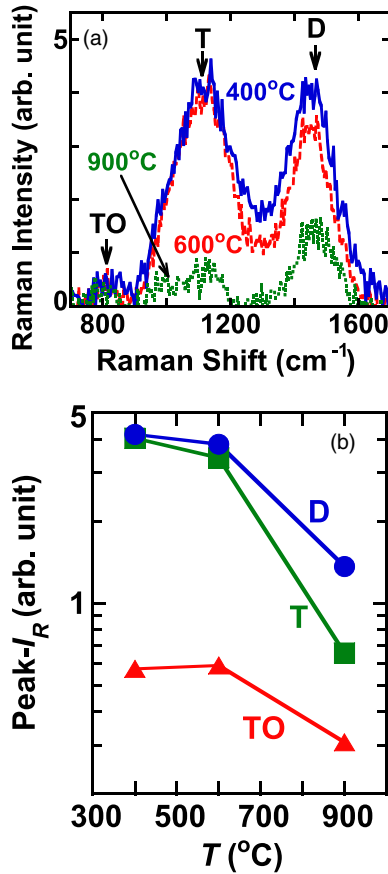


Fig. 8. (Color online) T dependence of (a) UV-Raman spectra of $\text{Si}^+/\text{C}^+-\text{OX}$ and (b) each peak Raman intensity of TO (triangles), T (squares), and D-bands (circles), where $D_S = 6 \times 10^{16} \text{ cm}^{-2}$, $D_C = 4 \times 10^{16} \text{ cm}^{-2}$ and $t_N = 0$. The Raman intensity is almost independent of T at $T \leq 600 \text{ }^\circ\text{C}$, but rapidly decreases at $T = 900 \text{ }^\circ\text{C}$. The Raman peak positions of each band are independent of T .

Raman peak intensities decrease at $t_N \geq 10$ min, whose mechanism is discussed after Fig. 10(b). On the other hand, Fig. 9(b) shows that with increasing t_N , T-band Raman position increases, which is attributable to the reduction of sp^3 site fraction in a-C and thus the increase of sp^2 phase⁴⁵⁾ after long N_2 annealing. However, the Raman shift positions of D-band and TO-mode are almost independent of t_N .

Next, we compare the UV-Raman between $\text{Si}^+/\text{C}^+-\text{OX}$ and C^+-OX . Figure 10(a) shows the Raman spectra of C^+-OX at t_N of 0 (solid line) and 5 min (dotted line), where $T = 600 \text{ }^\circ\text{C}$ and $D_C = 4 \times 10^{16} \text{ cm}^{-2}$, which indicates the typical Raman spectrum of a-C including T, D-band, and the G-band of graphite (sp^2 site).⁴⁵⁾ As expected, the TO mode of Si-C vibration cannot be observed in C^+-OX , because SiC is not formed in C^+-OX . G-band formation is the characteristic of C^+-OX , while $\text{Si}^+/\text{C}^+-\text{OX}$ shows no G-band, as shown in Figs. 7, 8(a), and 10(a). The I_R of $\text{Si}^+/\text{C}^+-\text{OX}$ at $t_N = 0$ (dashed line) is much smaller than that of C^+-OX , and for example, the I_D of $\text{Si}^+/\text{C}^+-\text{OX}$ is approximately 1/3 of that of C^+-OX at t_N of 0. As shown as XPS data in Fig. 3(a) for $\text{Si}^+/\text{C}^+-\text{OX}$, 80% of implanted C atoms forms SiC shown as Si-C bond and only 20% of C atoms forms a-C area shown as C-C bond, resulting in lower Raman intensity of a-C in $\text{Si}^+/\text{C}^+-\text{OX}$, as shown in Fig. 10(a). Figure 10(b) shows the t_N dependence of each peak Raman intensity of C^+-OX at the same process conditions of Fig. 10(a), and that all peak- I_R rapidly increases at $t_N = 5$ min, whose mechanism is

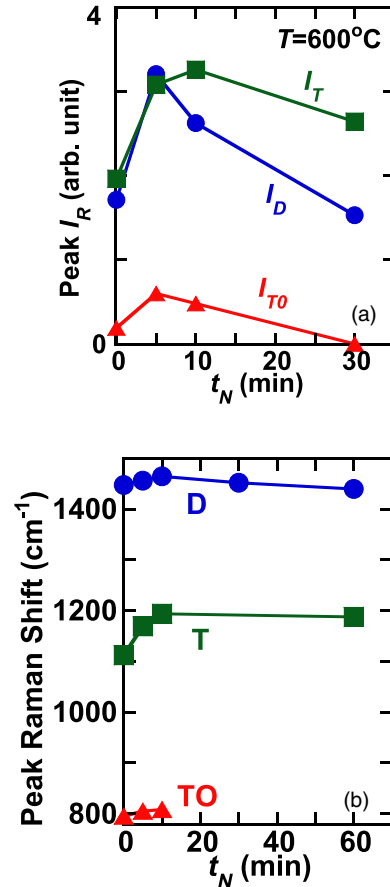


Fig. 9. (Color online) t_N dependence of peak Raman intensities of (a) I_D (circles), I_T (squares), and I_{TO} (triangles), and (b) peak Raman shifts of D- (circles), T- (squares), and TO-bands (triangles), where $T = 600 \text{ }^\circ\text{C}$, $D_S = 6 \times 10^{16} \text{ cm}^{-2}$, and $D_C = 4 \times 10^{16} \text{ cm}^{-2}$. All Raman peak intensities rapidly increase at $t_N \approx 5$ min, and then decrease after N_2 annealing at $t_N \geq 10$ min. The peak Raman shift of T-band strongly depends on t_N , but the peak Raman shift of D- and TO-bands are almost independent of t_N .

the same shown in Fig. 9(b). However, all peak- I_R keeps constant even at $t > 5$ min, which is much different from that of $\text{Si}^+/\text{C}^+-\text{OX}$ shown in Fig. 9(b). Thus, Fig. 10(b) data suggests that a-C volume is not reduced by the out-diffusion of C atoms from the SOX during high T_N annealing. As a result, the decrease of peak I_D and I_T of $\text{Si}^+/\text{C}^+-\text{OX}$ at $t_N \geq 10$ min, shown in Fig. 9(b), indicates that C atoms are excessed by the a-C volume reduction during high T_N annealing only in $\text{Si}^+/\text{C}^+-\text{OX}$, which possibly leads to the increase of Si-C bond, that is SiC formation enhancement, as shown as the rapid SiC-dot formation after N_2 annealing as the HAADF-STEM observation in Figs. 5(a) and 5(b). Thus, this SiC formation enhancement probably has a great influence on the t_N dependence of the PL properties of $\text{Si}^+/\text{C}^+-\text{OX}$ discussed in the next subsection. However, this SiC formation enhancement is not inconsistent with the I_{TO} reduction at long t_N shown in Fig. 9(a). Namely, the TO-band Raman intensity of SiC-dots decreases with reducing the SiC-dot diameter,²⁰⁾ because the SiC-dot diameter is considered to decrease after N_2 annealing even in SOX layer, similar to that in C^+-Si .⁴⁰⁾

3.3. PL properties

In this subsection, we mainly discuss the PL properties of $\text{Si}^+/\text{C}^+-\text{OX}$, comparing with those of C^+-Si .

3.3.1. Model for PL intensity from SiC-dots in oxide ($\text{Si}^+/\text{C}^+-\text{OX}$) and in Si (C^+-Si). Firstly, in this subsection,

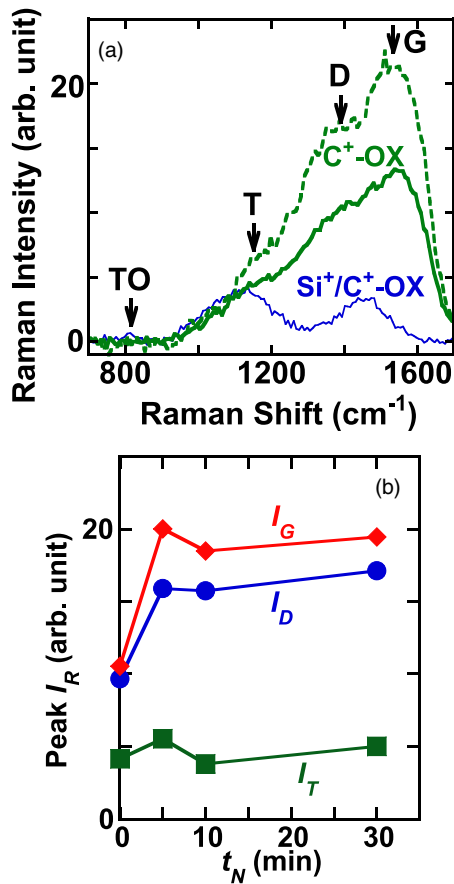


Fig. 10. (Color online) (a) UV-Raman spectra of C⁺-OX at $t_N = 0$ (solid line) and at $t_N = 5$ min (dashed line) and Si⁺/C⁺-OX (thin solid line) at $D_S = 6 \times 10^{16} \text{ cm}^{-2}$ and $t_N = 0$, and (b) t_N dependence of peak Raman intensities of I_T , I_D , and I_G of C⁺-OX, where $T = 600 \text{ }^\circ\text{C}$ $D_C = 4 \times 10^{16} \text{ cm}^{-2}$. The arrows in Fig. 10(a) show the G (observed in only C⁺-OX), D, T bands of C-C vibration, and TO-mode of Si-C vibration. The Raman intensity of C⁺-OX is much higher than that of Si⁺/C⁺-OX. Figure 10(b) shows that all peak I_D (circles), I_T (squares), and I_G (rhombi) rapidly increase at $t_N \approx 5$ min, similar to Fig. 9(b), but does not decrease after long N_2 annealing at $t_N > 5$ min.

we discuss the model for PL intensity from SiC-dots in Si⁺/C⁺-OX and C⁺-Si.

When the incident laser flux at the depth x from the material surface is $I_{EX}(x)$, $I_{EX}(x) = I_0 \exp(-x/\lambda_{EX})$,⁴¹⁾ where I_0 is the laser flux at the material surface and λ_{EX} is the penetration length of laser photons in the material layer. Assuming that the density of SiC dots is uniform N_S in a SiC-dot forming region in the range of x_1 to x_2 from the surface, I_{PL} from SiC-dots is proportional to the total area of SiC-dots; A_T in a unit area. In the case of SiC dots in SiO₂ (Si⁺/C⁺-OX), as discussed in Sect. 2, $\lambda_{EX} \approx \infty$, and thus $I_{EX}(x) = I_0$. Thus, the I_{PL} from SiC-dots in Si⁺/C⁺-OX can be given by the following equation^{38,40)}

$$I_{PL} = \eta_{OX} A_T \int_{x_1}^{x_2} I_{EX}(x) dx = \eta_{OX} \pi \left(\frac{R}{2} \right)^2 \times N_S I_0 (x_2 - x_1) = \eta_{OX} I_0 A_{TO}, \quad (2)$$

where η_{OX} is the PL emission coefficient of SiC-dots in Si⁺/C⁺-OX, and the A_T of Si⁺/C⁺-OX; A_{TO} is given by the next equations. Moreover, the C-content depth profile of Si⁺/C⁺-OX, shown as the XPS data in Fig. 3(c), shows that the SiC-dot formation region width is $20 \leq x \leq 120$ nm, and

thus, $x_2 = 120$ nm and $x_1 = 20$ nm

$$A_{TO} = \pi \left(\frac{R}{2} \right)^2 N_S (x_2 - x_1), \quad (3)$$

$$x_2 - x_1 \approx 100 \text{ nm}. \quad (4)$$

On the other hand, in the case of SiC dots in C⁺-Si, the C-content profile of C⁺-Si shown in Fig. 4 and TEM observation⁴⁰⁾ show that $x_2 = 50$ nm and $x_1 = 0$. In addition, the λ_{EX} of 325 nm photon in Si layer is approximately 8 nm.⁴¹⁾ Therefore, the I_{PL} from SiC-dots in c-Si (C⁺-Si) can be given by the following equation

$$\begin{aligned} I_{PL} &= \eta_{Si} A_T \int_{x_1}^{x_2} I_0 \exp\left(-\frac{x}{\lambda_{EX}}\right) dx \\ &= \eta_{Si} \pi \left(\frac{R}{2} \right)^2 N_S I_0 \lambda_{EX} \left(1 - \exp\left(-\frac{x_2}{\lambda_{EX}}\right) \right) \\ &\approx \eta_{Si} \pi \left(\frac{R}{2} \right)^2 N_S I_0 \lambda_{EX} = \eta_{Si} I_0 A_{TS}, \end{aligned} \quad (5)$$

where η_{Si} is the PL emission coefficient of SiC-dots in Si, $\exp(-x_2/\lambda_{EX}) \approx 0$, and the A_T of C⁺-Si; A_{TS} is given by the next equations

$$A_{TS} = \pi \left(\frac{R}{2} \right)^2 N_S \lambda_{EX}, \quad (6)$$

$$\lambda_{EX} \approx 8 \text{ nm}. \quad (7)$$

3.3.2. Double Si⁺/C⁺ hot-ion implantation effects on PL properties. Firstly, we discuss the influence of double Si⁺/C⁺ hot-ion implantation on PL properties of SiC-dots in Si⁺/C⁺-OX, comparing with those of C⁺-OX and Si⁺-OX.

Under the each optimum process conditions of three structures of Si⁺/C⁺-OX, C⁺-OX, and Si⁺-OX, Fig. 11 shows PL spectrum comparison between three structures of Si⁺/C⁺-OX (solid line) at $D_S = 6 \times 10^{16} \text{ cm}^{-2}$ and $D_C = 4 \times 10^{16} \text{ cm}^{-2}$, C⁺-OX (dashed line) at $D_C = 4 \times 10^{16} \text{ cm}^{-2}$, and Si⁺-OX (dotted line) at $D_S = 6 \times 10^{16} \text{ cm}^{-2}$, where $T = 600 \text{ }^\circ\text{C}$ and $t_N = 30$ min. We successfully observed the PL emissions from Si⁺/C⁺-OX and C⁺-OX which shows very broad with the photon energy range from 1.6 to 3.5 eV, while the PL intensity I_{PL} of Si⁺-OX is negligibly small in the photon energy range of higher than 1.6 eV even at the same D_S of Si⁺/C⁺-OX. Even under the same D_C , we demonstrated that the I_{PL} of Si⁺/C⁺-OX, which is emitted from SiC-QD, is much larger than that of C⁺-OX, and is approximately 9.3 times as large as that of C⁺-OX, while the very broad PL spectrum of C⁺-OX is typical for a-C.⁴⁸⁾ Thus, the key point, to achieve strong PL emission, is the realization of SiC-QD of Si⁺/C⁺-OX fabricated by double hot Si⁺/C⁺ ion implantation technique.

Next, we discuss the hot-ion implantation temperature T dependence of PL properties. Figures 12(a) and 12(b) show the T dependence of PL spectrum of Si⁺/C⁺-OX at $t_N = 0$ and 30 min, respectively, where $D_S = 6 \times 10^{16} \text{ cm}^{-2}$ and $D_C = 4 \times 10^{16} \text{ cm}^{-2}$. PL intensity increases with decreasing T under both t_N conditions. Before N_2 annealing at $t_N = 0$, Fig. 12(a) shows that the PL spectrum line shape strongly depend on T , the FWHM of PL spectrum decreases with decreasing T , and the E_{PH} increases from 2.0 to 2.5 eV with increasing T , which is discussed in detail in Figs. 14(b) and

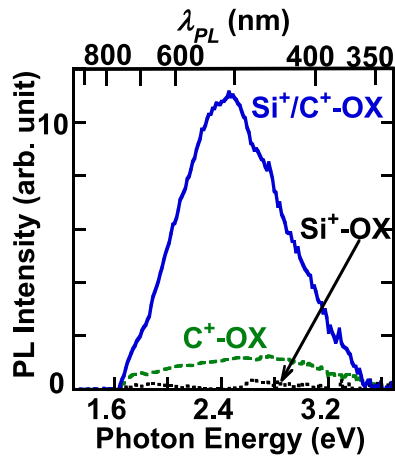


Fig. 11. (Color online) PL spectrum comparison between three structures of Si⁺/C⁺-OX (solid line) at $D_S = 6 \times 10^{16} \text{ cm}^{-2}$ and $D_C = 4 \times 10^{16} \text{ cm}^{-2}$, C⁺-OX (dashed line) at $D_C = 4 \times 10^{16} \text{ cm}^{-2}$, and Si⁺-OX (dotted line) at $D_S = 6 \times 10^{16} \text{ cm}^{-2}$, where $T = 600 \text{ }^\circ\text{C}$ and $t_N = 30 \text{ min}$. PL emission is successfully observed from SiC-dots in SOX. The PL intensity of Si⁺/C⁺-OX is much stronger than that of C⁺-OX, whereas the PL intensity of Si⁺-OX is negligibly small.

15(b). However, after N₂ annealing, Fig. 12(b) shows that the PL spectrum line shape is almost independent of T , and the E_{PH} at $T = 400 \text{ }^\circ\text{C}$ and $600 \text{ }^\circ\text{C}$ are approximately 2.43 eV and 2.45 eV, respectively, which are almost the same E_G of 3C-SiC (2.4 eV).^{20,21)} Therefore, the polytype of SiC-dots of Si⁺/C⁺-OX, after N₂ annealing, are also identified as 3C-SiC by PL spectrum as well as CSTEM images in Figs. 6(a) and 6(b). As a result, before N₂ annealing shown in Fig. 12(a), the E_{PH} of lower than 2.4 eV at $T = 400 \text{ }^\circ\text{C}$ and $600 \text{ }^\circ\text{C}$ is possibly attributable to PL emission from Si-C alloy, as shown in hot-C-ion implanted a-Si.³⁸⁾ On the other hand, Fig. 12(c) shows the t_N dependence of I_{MAX} of Si⁺/C⁺-OX at $T = 400 \text{ }^\circ\text{C}$ (circles), $600 \text{ }^\circ\text{C}$ (squares), and $900 \text{ }^\circ\text{C}$ (triangles). I_{MAX} suddenly increases at $t_N = 5 \text{ min}$, which is attributable to the rapid SiC-dot formation, as discussed in HAADF-STEM [Figs. 5(a)–5(b)], CSTEM [Figs. 6(a)–6(b)], and Figs. 10(a)–10(b). For example, the I_{MAX} enhancement factor at $t_N = 5 \text{ min}$, compared with I_{MAX} at $t_N = 0$, reaches 12.7 at $T = 400 \text{ }^\circ\text{C}$, which is much larger than the I_{MAX} enhancement factor of C⁺-Si (≈ 3.8).⁴⁰⁾ Thus, the post N₂ annealing for Si⁺/C⁺-OX is very effective for improving I_{PL} . However, the I_{MAX} is almost saturated at $t_N > 10 \text{ min}$. In the whole range of t_N , the I_{MAX} at $T = 400 \text{ }^\circ\text{C}$ has the maximum value, and thus, it is concluded that the optimum T for improving I_{PL} is about $400 \text{ }^\circ\text{C}$ in Si⁺/C⁺-OX.

Here, we discuss the physical mechanism for the T dependence of I_{MAX} . Equation (2) shows that $I_{MAX} \propto A_{TO}$ for Si⁺/C⁺-OX. Using the R and N data of $T = 400 \text{ }^\circ\text{C}$ and $600 \text{ }^\circ\text{C}$ shown in Fig. 5(d), the N_S of $T = 400 \text{ }^\circ\text{C}$ and $600 \text{ }^\circ\text{C}$ are approximately 1.7×10^{18} and $3.4 \times 10^{17} \text{ cm}^{-3}$, respectively. Therefore, the A_{TO} at $T = 400 \text{ }^\circ\text{C}$ and $600 \text{ }^\circ\text{C}$ can be calculated by Eq. (3) and are estimated to be 0.54 and 0.43, respectively. As a result, Fig. 12(d) shows I_{MAX} versus A_{TO} of Eq. (3) at $T = 400 \text{ }^\circ\text{C}$ (circle) and $600 \text{ }^\circ\text{C}$ (square), as the same data of Fig. 12(b). Dashed line is the linear fitting curve for experimental data, and the experimental I_{MAX} data can be well fitted by $I_{MAX} \propto A_{TO}$ of Eq. (2) with the correlation

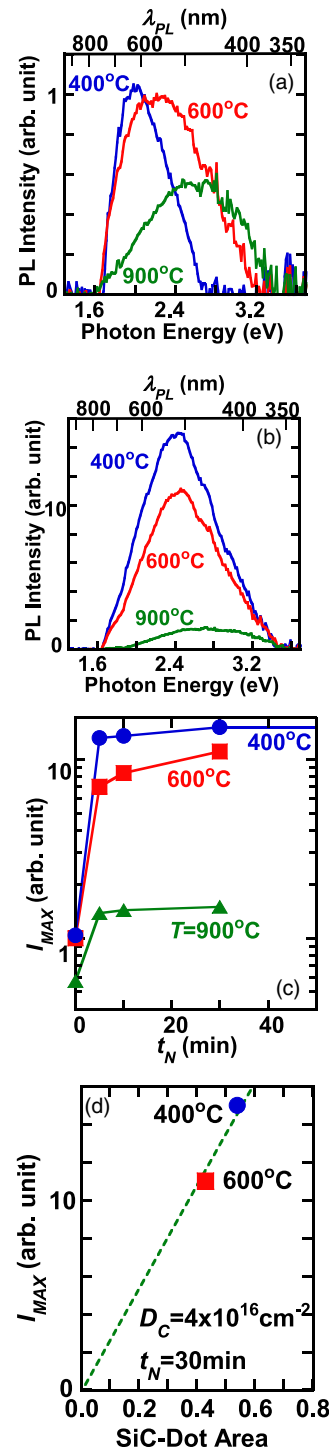


Fig. 12. (Color online) T dependence of PL spectrum at (a) $t_N = 0$ and (b) 30 min, where $D_S = 6 \times 10^{16} \text{ cm}^{-2}$ and $D_C = 4 \times 10^{16} \text{ cm}^{-2}$. PL intensity drastically increases after N₂ annealing and with decreasing T . Figure 12(a) at $t_N = 0$ shows that the PL spectrum line shape strongly depend on T , but Fig. 12(b) at $t_N = 30 \text{ min}$ shows that the PL spectrum line shape is almost independent of T . (c) t_N dependence of I_{MAX} of Si⁺/C⁺-OX at $T = 400 \text{ }^\circ\text{C}$ (circles), $600 \text{ }^\circ\text{C}$ (squares), and $900 \text{ }^\circ\text{C}$ (triangles), where $D_S = 6 \times 10^{16} \text{ cm}^{-2}$ and $D_C = 4 \times 10^{16} \text{ cm}^{-2}$. I_{MAX} suddenly increases at $t_N = 5 \text{ min}$, and slightly increases with increasing t_N at $t_N \geq 10 \text{ min}$. In the whole range of t_N , the I_{MAX} at $T = 400 \text{ }^\circ\text{C}$ shows the maximum. (d) I_{MAX} of Fig. 12(b) versus total SiC dot area A_{TO} of Eq. (3) at $T = 400 \text{ }^\circ\text{C}$ (circle) and $600 \text{ }^\circ\text{C}$ (square), where the dashed line is the linear fitting curve of data. Figure 12(d) shows that experimental I_{MAX} can be well fitted by the relation of $I_{MAX} \propto A_{TO}$ of Eq. (2) with the correlation coefficient of nearly unity, and thus the PL intensity enhancement at $T = 400 \text{ }^\circ\text{C}$ is attributable to the increase of A_{TO} at $T = 400 \text{ }^\circ\text{C}$.

coefficient of nearly unity. As a result, Fig. 12(d) shows that the larger I_{MAX} at $T = 400^\circ\text{C}$, compared with that at $T = 600^\circ\text{C}$, shown in Figs. 12(b) and 12(c), is attributable to the increase of total SiC dot area A_{TO} at $T = 400^\circ\text{C}$. Therefore, the η_{OX} of Eq. (2) is almost independent of T , and thus the η_{OX} is independent of R shown under $400^\circ\text{C} \leq T \leq 600^\circ\text{C}$ in Fig. 5(d). Consequently, the PL intensity model for $\text{Si}^+/\text{C}^+-\text{OX}$ discussed in Sect. 3.3.1 is experimentally confirmed by Fig. 12(d).

Next, Figs. 13(a) and 13(b) show the D_C dependence of UV-Raman spectrum at $t_N = 0$ and PL spectrum at $t_N = 30$ min, respectively, where $T = 600^\circ\text{C}$. The solid and dashed lines show the data of low ion-doses of $D_S = 6 \times 10^{16} \text{ cm}^{-2}$ and $D_C = 4 \times 10^{16} \text{ cm}^{-2}$, and high ion-doses of $D_S = 1 \times 10^{17} \text{ cm}^{-2}$ and $D_C = 6 \times 10^{16} \text{ cm}^{-2}$, respectively. Figure 13(a) shows that Raman spectrum line shape is almost independent of D_C , but the Raman intensity slightly increases with increasing D_C , which suggests that a-C formation rate increases with increasing D_C . On the other hand, Fig. 13(b) shows that the PL spectrum line shape is independent of D_C , but the PL intensity decreases with increasing D_C , which is possibly attributable to the defect increase of SiC-dots at high ion-dose conditions of D_S and D_C . Thus, for improving I_{PL} , the low ion-dose conditions is better than the high ion-dose conditions in this study.

3.3.3. PL comparison between $\text{Si}^+/\text{C}^+-\text{OX}$ and C^+-Si . In this subsection, we compare the PL properties of $\text{Si}^+/\text{C}^+-\text{OX}$ with those of C^+-OX and C^+-Si at each optimum process

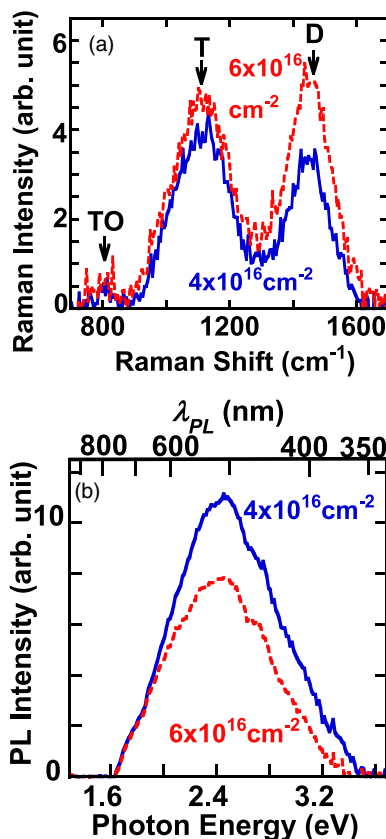


Fig. 13. (Color online) D_C dependence of (a) UV-Raman spectrum at $t_N = 0$ min and (b) PL spectrum at $t_N = 30$ min, where $T = 600^\circ\text{C}$, and the D_S of low ion-dose of $D_C = 4 \times 10^{16}$ (circles) and of high ion-dose of $6 \times 10^{16} \text{ cm}^{-2}$ (triangles) are 6×10^{16} and $1 \times 10^{17} \text{ cm}^{-2}$, respectively. Figure 13(a) shows that the Raman intensity increases with increasing D_C , but Fig. 13(b) shows that the PL intensity decreases with increasing D_C .

conditions. Namely, the optimum T for $\text{Si}^+/\text{C}^+-\text{OX}$ is 400°C , as shown in Fig. 12.

Figures 14(a) and 14(b) show the PL spectra before and after N_2 annealing, respectively, where $D_C = 4 \times 10^{16} \text{ cm}^{-2}$. Solid, dashed, and dotted lines show the data of $\text{Si}^+/\text{C}^+-\text{OX}$ at $T = 400^\circ\text{C}$ and $D_S = 6 \times 10^{16} \text{ cm}^{-2}$, C^+-Si at $T = 600^\circ\text{C}$, and C^+-OX at $T = 600^\circ\text{C}$, respectively. The t_N of $\text{Si}^+/\text{C}^+-\text{OX}$, C^+-Si , and C^+-OX in Fig. 14(b) are 30, 5, and 30 min, respectively. Figure 14(a) shows that before N_2 annealing, the PL intensity of $\text{Si}^+/\text{C}^+-\text{OX}$ is 66% of that of C^+-Si , but is 2.1 times larger than that of C^+-OX . The PL spectrum line shape of $\text{Si}^+/\text{C}^+-\text{OX}$ before N_2 annealing is much different from that of C^+-Si , and thus, the E_{PH} of $\text{Si}^+/\text{C}^+-\text{OX}$ (2.0 eV) is 0.9 eV lower than that of C^+-Si (2.9 eV), but is almost the same as that of C^+-OX (2.2 eV). However, after N_2 annealing, Fig. 14(b) shows that the PL intensity of $\text{Si}^+/\text{C}^+-\text{OX}$ is drastically enhanced, as discussed in Fig. 12(b), and the E_{PH} of $\text{Si}^+/\text{C}^+-\text{OX}$ increases to 2.4 eV. As a result, the I_{MAX} of $\text{Si}^+/\text{C}^+-\text{OX}$ is approximately 2.6 and 12 times larger than those of C^+-Si and C^+-OX , respectively. Therefore, the double hot-ion implantation into SOX

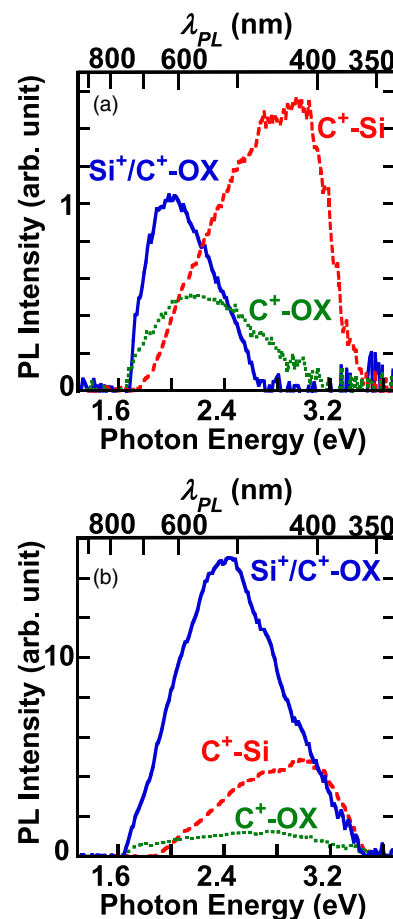


Fig. 14. (Color online) Three structure dependence of PL spectrum at each optimum conditions (a) before and (b) after N_2 annealing, where $D_C = 4 \times 10^{16} \text{ cm}^{-2}$. Solid, dashed, and dotted lines show the data of $\text{Si}^+/\text{C}^+-\text{OX}$ at $T = 400^\circ\text{C}$ and $D_S = 6 \times 10^{16} \text{ cm}^{-2}$, C^+-Si at $T = 600^\circ\text{C}$, and C^+-OX at $T = 600^\circ\text{C}$, respectively. The t_N of $\text{Si}^+/\text{C}^+-\text{OX}$, C^+-Si , and C^+-OX in (b) are 30, 5, and 30 min, respectively. Figure 14(a) shows that before N_2 annealing, the PL intensity of C^+-Si is the maximum, but Fig. 14(b) shows that the PL intensity of $\text{Si}^+/\text{C}^+-\text{OX}$ is drastically enhanced after N_2 annealing, resulting in the maximum PL intensity between three structures.

layer and the post N₂ annealing are the key processes for improving PL intensity.

Next, Figs. 15(a) and 15(b) show the t_N dependence of I_{MAX} and E_{PH} of three structures shown in Fig. 14, respectively, at the same process conditions of Figs. 14(a) and 14(b). Namely, circles, triangles, and squares show the data of Si⁺/C⁺-OX at $T = 400$ °C and $D_S = 6 \times 10^{16}$ cm⁻², C⁺-Si at $T = 600$ °C, and C⁺-OX at $T = 600$ °C, respectively, where $D_C = 4 \times 10^{16}$ cm⁻². Figure 15(a) shows that the I_{MAX} of all structures rapidly increases at $t_N = 5$ min, and especially, the t_N dependence of I_{MAX} of Si⁺/C⁺-OX is much larger than those of C⁺-Si and C⁺-OX, which is the characteristic of Si⁺/C⁺-OX. Thus, the I_{MAX} of Si⁺/C⁺-OX is the largest in three structures after N₂ annealing. Moreover, the I_{MAX} of Si⁺/C⁺-OX and C⁺-OX gradually increases with increasing t_N even at $t_N > 5$ min, whereas the I_{MAX} of C⁺-Si slowly decreases with increasing t_N at $t_N > 5$ min. On the other hand, Fig. 15(b) shows that the E_{PH} of Si⁺/C⁺-OX and C⁺-OX are much lower than that of C⁺-Si, suddenly increases at $t_N = 5$ min, and is almost saturated $t_N > 5$ min. The E_{PH} increases of Si⁺/C⁺-OX and C⁺-OX after N₂ annealing reach 0.47 and 0.54 eV, respectively. This E_{PH} increase to 2.4 eV in Si⁺/C⁺-OX is possibly attributable to the 3C-SiC dot formation at $t_N = 5$ min, which is already discussed in Figs. 6 and 12. However, the E_{PH} shift of C⁺-Si is within the error range and the E_{PH} is almost independent of t_N . Figure 15(c) shows the relationship between I_{MAX} and E_{PH} of the same data in Figs. 15(a) and 15(b). The I_{MAX} of Si⁺/C⁺-OX and C⁺-OX have the positive correlation with E_{PH} , and it is possibly expressed that $I_{MAX} \propto e^{E_{PH}/E_0}$ shown as fitting dashed and dotted lines, where E_0 is a fitting parameter. In this study, the E_0 of Si⁺/C⁺-OX and C⁺-OX are approximately 0.17 and 0.72 eV, respectively, whose physical meaning is not understood at present.

Moreover, Figs. 16(a) and 16(b) show the T dependence of I_{MAX} and E_{PH} of Si⁺/C⁺-OX (circles) and C⁺-Si⁴⁰) (triangles), respectively, at the same process conditions of Fig. 14. Solid and dashed lines show the data after and before N₂ annealing, respectively. Figure 16(a) shows that the I_{MAX} of Si⁺/C⁺-OX has the maximum value at $T = 400$ °C, and is much higher than that of C⁺-Si at $T \leq 600$ °C after N₂ annealing. However, before N₂ annealing, the I_{MAX} of Si⁺/C⁺-OX is almost the same as that of C⁺-Si. On the other hand, the I_{MAX} of C⁺-Si has the maximum value at $T = 600$ °C, which is 200 °C higher than that of Si⁺/C⁺-OX. Figure 16(b) shows that the E_{PH} of Si⁺/C⁺-OX is much lower than that of C⁺-Si at $T \leq 900$ °C. Before N₂ annealing, the E_{PH} of both structures increases with increasing T , and the maximum E_{PH} increases of Si⁺/C⁺-OX and C⁺-Si are approximately 0.55 and 0.36 eV by T increase, respectively. Thus, thermal processes of hot-ion implantation, as well as N₂ annealing shown in Fig. 15(b), causes the E_{PH} increase of Si⁺/C⁺-OX. Especially, even before N₂ annealing, the E_{PH} of Si⁺/C⁺-OX is almost equal to the E_G of 3C-SiC (2.4 eV) at $T = 900$ °C. Therefore, high-temperature thermal processes (hot-ion implantation and N₂ annealing) lead to a SiC-dot (such as 3C-SiC) formation in Si⁺/C⁺-OX.

3.3.4. QD effects on PL properties of Si⁺/C⁺-OX. In this subsection, we discuss QD-effects on PL intensity of Si⁺/C⁺-OX compared to that of C⁺-Si at each optimum process conditions to improve PL intensity shown in

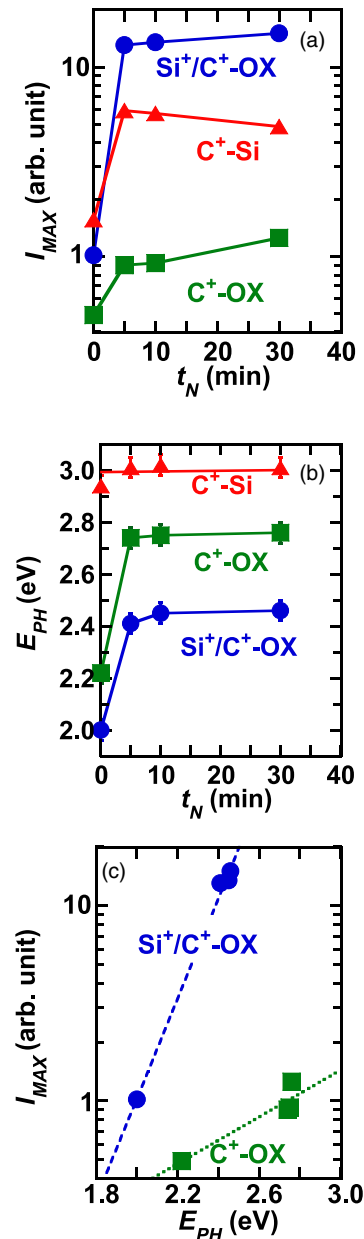


Fig. 15. (Color online) t_N dependence of (a) I_{MAX} and (b) E_{PH} of three structures, where $D_C = 4 \times 10^{16}$ cm⁻². Circles, triangles, and squares show the data of Si⁺/C⁺-OX at $T = 400$ °C and $D_S = 6 \times 10^{16}$ cm⁻², C⁺-Si at $T = 600$ °C, and C⁺-OX at $T = 600$ °C, respectively. Figure 15(a) shows that the I_{MAX} of Si⁺/C⁺-OX is much stronger than those of Si⁺/C⁺-OX and C⁺-OX, respectively. On the other hand, Fig. 15(b) shows that the E_{PH} of Si⁺/C⁺-OX and C⁺-OX are much lower than that of C⁺-Si and rapidly increase at $t_N = 5$ min. (c) I_{MAX} versus E_{PH} of the same data of Si⁺/C⁺-OX (circles) and C⁺-OX (squares) in Fig. 15(b). The I_{MAX} of Si⁺/C⁺-OX and C⁺-OX have the positive correlation with the E_{PH} , and it is possibly expressed that $I_{MAX} \propto e^{E_{PH}/E_0}$ shown as dashed and dotted lines, where E_0 is a fitting parameter.

Figs. 14(b) and 15(a), using the PL model discussed in Sect. 3.3.1. Namely, we compare the PL emission coefficient between η_{OX} (Si⁺/C⁺-OX) in Eq. (2) and η_{Si} (C⁺-Si) in Eq. (5).

The total SiC-dot area of Si⁺/C⁺-OX; A_{TO} in Eqs. (3) and (4) can be obtained by HAADF-STEM data in Fig. 5(d), where $R \approx 2$ nm and $N_S \approx 2 \times 10^{18}$ cm⁻³. On the other hand, the total SiC-dot area of C⁺-Si; A_{TS} in Eqs. (6) and (7) can be obtained by the C-content profile of C⁺-Si shown in Fig. 4

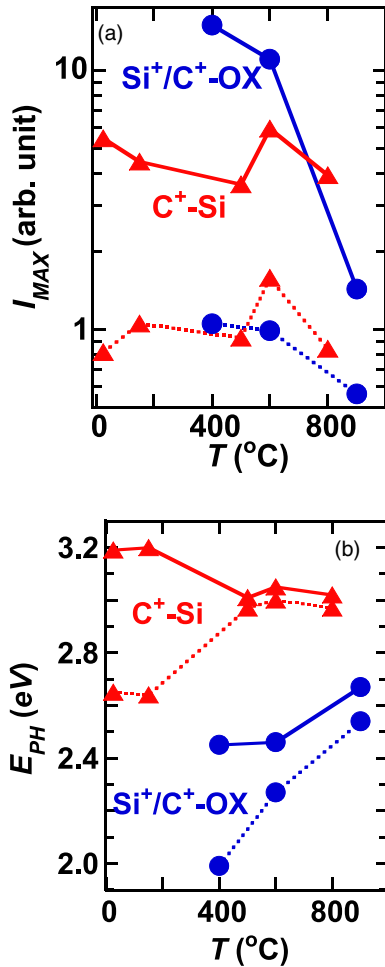


Fig. 16. (Color online) T dependence of (a) I_{MAX} and (b) E_{PH} of $Si^{+}/C^{+}-OX$ (circles) and $C^{+}-Si$ (triangles) at the same process conditions of Fig. 14(b). Solid and dashed lines show the data after and before N_2 annealing, respectively, where the t_N of $Si^{+}/C^{+}-OX$ and $C^{+}-Si$ after N_2 annealing are 30 and 5 min, respectively. Figure 16(a) shows that the I_{MAX} of $Si^{+}/C^{+}-OX$ has the maximum value at $T = 400$ °C, and is much higher than that of $C^{+}-Si$ in the range of $T \leq 600$ °C. However, the I_{MAX} of $C^{+}-Si$ has the maximum value at $T = 600$ °C. Figure 16(b) shows that the E_{PH} of $Si^{+}/C^{+}-OX$ is lower than that of $C^{+}-Si$ at $T \leq 800$ °C, and that the E_{PH} of $Si^{+}/C^{+}-OX$ before N_2 annealing drastically increases with increasing T .

and TEM observation,⁴⁰ where $x_2 = 50$ nm, $x_l = 0$, $R \approx 3$ nm, $N_S \approx 8 \times 10^{18}$ cm⁻³, and $\lambda_{EX} \approx 8$ nm.⁴¹ As a result, Eqs. (3) and (6) show that the thickness of SiC-dot emission volume of $Si^{+}/C^{+}-OX$ is 100 nm ($=x_2-x_l$), which is 12.5 times thicker than that of $C^{+}-Si$ ($=\lambda_{EX} = 8$ nm). However, the R of $Si^{+}/C^{+}-OX$ (≈ 2 nm) is 1/2 of that of $C^{+}-Si$ (≈ 4 nm), and the N_S of $Si^{+}/C^{+}-OX$ ($\approx 2 \times 10^{18}$ cm⁻³) is only 1/4 of that of $C^{+}-Si$ ($\approx 8 \times 10^{18}$ cm⁻³). As a result, the total SiC-dot area shown in Eqs. (3) and (6) show that $A_{TO} \approx 0.5$ and $A_{TS} \approx 0.5$, resulting in $A_{TO} \approx A_{TS}$. Therefore, this is the advantageous characteristics of $Si^{+}/C^{+}-OX$ that can emit the PL photons from all SiC-dots in the whole thickness of SiO_2 layer, in spite of lower N_S of $Si^{+}/C^{+}-OX$.

Here, Fig. 17 shows experimental I_{MAX} versus A_{TO} (circle) at $D_S = 6 \times 10^{16}$ cm⁻², and experimental I_{MAX} versus A_{TS} (triangle), where the I_{MAX} is obtained by Fig. 14(b) data. At the same total SiC-dot area, the I_{MAX} of $Si^{+}/C^{+}-OX$ is 2.5 times larger than that of $C^{+}-Si$. This I_{MAX} enhancement of $Si^{+}/C^{+}-OX$ (≈ 2.5), compared with the I_{MAX} of $C^{+}-Si$, is considered to be due to the η improvement η_{OX}/η_{Si} in

$Si^{+}/C^{+}-OX$, which is possibly attributable to the QD effect on PL coefficient enhancement in $Si^{+}/C^{+}-OX$.

4. Conclusion

In this work, we experimentally studied SiC QD in SiO_2 with larger E_G (9 eV) ($Si^{+}/C^{+}-OX$) fabricated by the double hot- Si^{+}/C^{+} implantation into an oxide layer in various hot-ion implantation conditions and the post N_2 annealing at $T_N = 1000$ °C, where 400 °C $\leq T \leq 900$ °C, $6 \times 10^{16} \leq D_S \leq 1 \times 10^{17}$ cm⁻², and $4 \times 10^{16} \leq D_C \leq 6 \times 10^{16}$ cm⁻². In addition, we compare the PL properties of $Si^{+}/C^{+}-OX$ with those of single hot- C^{+} implanted oxide ($C^{+}-OX$) and single hot- Si^{+} implanted oxide ($Si^{+}-OX$) as well as conventional single hot- C^{+} implanted c-Si ($C^{+}-Si$).

The C1s analysis of XPS confirms Si-C bond in SiO_2 (FWHM ≈ 60 nm), which is the direct verification of SiC formation even in SiO_2 layer. At $D_C = 4 \times 10^{16}$ cm⁻², the peak C-content of $Si^{+}/C^{+}-OX$ is approximately 4.3 at%, which is about 40% of that of $C^{+}-Si$. The C-C bond spectrum shows that C-atom separation is also observed only in the oxide layer. Moreover, we demonstrated the SiC-dot formation in SiO_2 of $Si^{+}/C^{+}-OX$ by HAADF-STEM and CSTEM observations, and the diameter R and surface density N of SiC-dots are approximately 2 nm and 1.4×10^{12} cm⁻² at $T = 400$ °C and $D_C = 4 \times 10^{16}$ cm⁻², respectively, and also depend on T . The CSTEM images show the linear lattice spots of SiC-dots even in SiO_2 , which suggests that main polytype of SiC-dots is 3C-SiC. Thus, the R of $Si^{+}/C^{+}-OX$ is 1/2 of $C^{+}-Si$ (≈ 3 nm). On the other hand, the N of $Si^{+}/C^{+}-OX$ are only 18% of that of $C^{+}-Si$.

We demonstrated very stronger PL intensity I_{PL} of $Si^{+}/C^{+}-OX$ in the UV/visible regions, compared with that of $C^{+}-OX$ and $Si^{+}-OX$. Therefore, the key point, to realize strong PL emission, is the double $-Si^{+}/C^{+}$ implantation into an oxide layer. In addition, the maximum I_{PL} ; I_{MAX} of $Si^{+}/C^{+}-OX$ is 2.6 times larger than that of $C^{+}-Si$ at each optimum process condition. The PL spectrum line shape of $Si^{+}/C^{+}-OX$ is much different from that of $C^{+}-Si$, and it is noted that the photon energy E_{PH} of $Si^{+}/C^{+}-OX$ rapidly

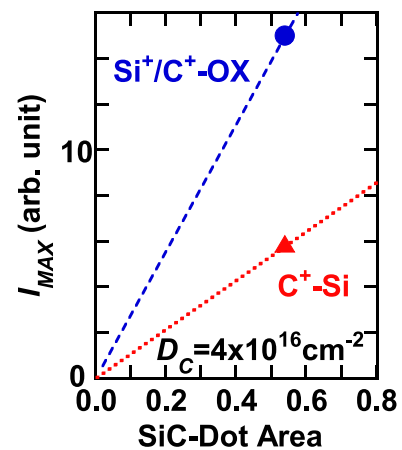


Fig. 17. (Color online) Experimental I_{MAX} of Fig. 14(b) as a function of total SiC-dot area of $Si^{+}/C^{+}-OX$ (circle) at the optimum conditions of $T = 400$ °C and $D_S = 6 \times 10^{16}$ cm⁻², and $C^{+}-Si$ (triangle) at the optimum conditions of $T = 600$ °C, where total SiC-dot areas of $Si^{+}/C^{+}-OX$ and $C^{+}-Si$ are calculated by Eqs. (3) and (6), respectively. At the same total SiC-dot area, the I_{MAX} of $Si^{+}/C^{+}-OX$ is approximately 2.5 times larger than that of $C^{+}-Si$, which is possibly attributable to QD effect on PL coefficient enhancement in $Si^{+}/C^{+}-OX$.

increases to approximately 2.4 eV with increasing the hot-ion implantation temperature T and N_2 annealing time t_N . Therefore, this E_{PH} of 2.4 eV also suggests that the polytype of SiC-dots in Si^+/C^+-OX is 3C-SiC. As a result, the I_{MAX} of Si^+/C^+-OX has the positive correlation with the E_{PH} , while in the case of C^+-Si , the correlation coefficient between I_{MAX} and E_{PH} is very weak. Moreover, we confirm that the I_{MAX} of Si^+/C^+-OX is proportional to the total SiC-dot area A_T calculated by R and N evaluated by HAADF-STEM, and as a result, the I_{MAX} increase at low- T can be explained by the increase of total SiC-dot area at low- T condition.

Moreover, we compare the PL emission coefficient η of Si^+/C^+-OX with that of C^+-Si , analyzing the relation between I_{MAX} and A_T . As a result, we experimentally verify that the PL emission coefficient of Si^+/C^+-OX is approximately 2.5 times larger than that of C^+-Si , which is possibly attributable to the QD-induced-increase of PL emission coefficient in Si^+/C^+-OX .

According to the above discussions, SiC-QD can be easily formed by double hot- Si^+/C^+ implantation into SiO_2 with higher E_G , and thus, a semiconductor layer is not essential for forming SiC-dots. Therefore, Si^+/C^+-OX technique can also produce SiC-QD at lower cost, and in addition, can improve PL intensity. Consequently, Si^+/C^+-OX technique is very promising for low-cost visible-photonic devices.

Acknowledgments

This work was partially supported by a Grant-in-Aid for Scientific Research from the Japan Society for the Promotion of Science (17K06359).

- 1) S. Saito et al., *Jpn. J. Appl. Phys.* **45**, L679 (2006).
- 2) S. Saito et al., *IEDM Technical Digest* (IEEE, Piscataway, NJ, 2008).
- 3) L. Pavesi and D. J. Lockwood, *Silicon Photonics* (Springer, Berlin, 2004).
- 4) T. Mizuno, K. Tobe, Y. Maruyama, and T. Sameshima, *Jpn. J. Appl. Phys.* **51**, 02BC03 (2012).
- 5) T. Mizuno, T. Aoki, Y. Nagata, Y. Nakahara, and T. Sameshima, *Jpn. J. Appl. Phys.* **52**, 04CC13 (2013).
- 6) T. Mizuno, Y. Nakahara, Y. Nagata, Y. Suzuki, T. Aoki, and T. Sameshima, *Jpn. J. Appl. Phys.* **53**, 04EC08 (2014).
- 7) T. Mizuno, Y. Nagata, Y. Suzuki, Y. Nakahara, T. Aoki, and T. Sameshima, *Jpn. J. Appl. Phys.* **53**, 04EC09 (2014).
- 8) T. Mizuno, Y. Nagamine, Y. Suzuki, Y. Nakahara, Y. Nagata, T. Aoki, and T. Sameshima, *Jpn. J. Appl. Phys.* **54**, 04DC05 (2015).
- 9) T. Mizuno, Y. Suzuki, Y. Nagamine, Y. Nakahara, Y. Nagata, T. Aoki, and T. Maeda, *Jpn. J. Appl. Phys.* **54**, 04DC02 (2015).
- 10) L. Donetti, F. Gámiz, J. B. Roldán, and A. Godoy, *J. Appl. Phys.* **100**, 013701 (2006).
- 11) K. Uchida, H. Watanabe, A. Kinoshita, J. Koga, T. Numata, and S. Takagi, *IEDM Tech. Dig.*, 2002, p. 47.
- 12) K. Uchida, J. Koga, and S. Takagi, *J. Appl. Phys.* **102**, 074510 (2007).
- 13) G. Tsutsui, M. Saitoh, and T. Hiramoto, *IEEE Trans. Electron Devices* **26**, 836 (2005).
- 14) B. K. Agrawal and S. Agrawal, *Appl. Phys. Lett.* **77**, 3039 (2000).
- 15) S. S. Iyer and Y.-H. Xie, *Science* **260**, 40 (1993).
- 16) A. Nazarov, J.-P. Colinge, F. Balestra, J.-P. Raskin, F. Gamiz, and V. S. Lysenko, *Semiconductor-On-Insulator Materials for Nanoelectronics Applications* (Springer, Berlin, 2011).
- 17) L. R. Tessler and I. Solomon, *Phys. Rev. B* **52**, 10962 (1995).
- 18) W. Liu, M. Zhang, C. Lin, Z. Zeng, L. Wang, and P. K. Chu, *Appl. Phys. Lett.* **78**, 37 (2001).
- 19) S. T. Pantelides and S. Zollner, *Silicon-Germanium Carbon Alloys* (Taylor & Francis, New York, 2002).
- 20) J. Fan and P. K. Chu, *Silicon Carbide Nanostructure* (Springer, Cham, 2014), Chaps. 3–7.
- 21) T. Kimoto and J. A. Cooper, *Fundamentals of Silicon Carbide Technology* (IEEE Press, Singapore, 2014), Chaps. 2, 5.
- 22) T. Kimoto, S. Nakazawa, K. Hashimoto, and H. Matsunami, *Appl. Phys. Lett.* **79**, 2761 (2001).
- 23) K. Adhikari and A. K. Ray, *J. Nanopart. Res.* **14**, 816 (2012).
- 24) S. Kim, J. E. Spanter, and I. P. Herman, *Jpn. J. Appl. Phys.* **39**, 5875 (2000).
- 25) T. V. Torchynska, A. D. Canoa, S. J. Sandoval, M. Dybicz, S. Ostapenkoc, and M. Mynbaevad, *Microelectron. J.* **36**, 536 (2005).
- 26) S. Lin, S. Zhang, X. Li, W. Xu, X. Pi, X. Liu, F. Wang, H. Wu, and H. Chen, *J. Phys. Chem. C* **119**, 19772 (2015).
- 27) E. Bekaroglu, M. Topsakal, S. Cahangirov, and S. Ciraci, *Phys. Rev. B* **81**, 075433 (2010).
- 28) G. Wei, W. Qin, G. Wang, J. Sun, J. Lin, R. Kim, D. Zhang, and K. Zheng, *J. Phys. D: Appl. Phys.* **41**, 235102 (2008).
- 29) L. Latu-Roman and M. Ollivier, *Silicon Carbide One-Dimensional Nanostructures* (Wiley, London, 2015).
- 30) J. A. Borders, S. T. Picraux, and W. Beezhold, *Appl. Phys. Lett.* **18**, 509 (1971).
- 31) Y. H. Gao, Z. Zhang, L. S. Liao, and X. M. Bao, *Appl. Phys. Lett.* **66**, 2382 (1995).
- 32) T. Mizuno, Y. Nagamine, Y. Omata, Y. Suzuki, W. Urayama, T. Aoki, and T. Sameshima, *Jpn. J. Appl. Phys.* **55**, 04EB02 (2016).
- 33) T. Mizuno, Y. Omata, Y. Nagamine, T. Aoki, and T. Sameshima, *Jpn. J. Appl. Phys.* **56**, 04CB03 (2017).
- 34) T. Mizuno, Y. Omata, S. Nakada, T. Aoki, and T. Sasaki, *Int. Conf. on Solid State Devices and Materials 2017: Extended Abstract of Solid State Devices and Materials, 2017* (Sendai, Japan), (The Japan Society of Applied Physics), p. 537.
- 35) T. Mizuno, Y. Omata, R. Kanazawa, Y. Iguchi, S. Nakada, T. Aoki, and T. Sasaki, *Jpn. J. Appl. Phys.* **57**, 04FB03 (2018).
- 36) Y. Shimizu et al., *Appl. Phys. Lett.* **98**, 232101 (2011).
- 37) Y. Shimizu, H. Takamizawa, K. Inoue, F. Yano, S. Kudo, A. Nishida, T. Toyama, and Y. Nagai, *Jpn. J. Appl. Phys.* **55**, 026501 (2016).
- 38) T. Mizuno, R. Kanazawa, Y. Omata, T. Aoki, and T. Sameshima, *Jpn. J. Appl. Phys.* **58**, SSBJ01 (2019).
- 39) T. Mizuno, M. Yamamoto, T. Aoki, and T. Sameshima, *Abstract of IEEE Silicon Nanoelectronics Workshop 2019, 2019* (IEEE), (Kyoto), p. 115.
- 40) T. Mizuno, M. Yamamoto, S. Nakada, S. Irie, T. Aoki, and T. Sameshima, *Jpn. J. Appl. Phys.*, **58**, 081004 (2019).
- 41) S. M. Sze and K. K. Ng, *Physics of Semiconductor Devices* (Wiley, New York, 2007), Chap. 1.
- 42) H. Li, J. Wu, and Z. M. Wang, *Silicon-Based Nanomaterials* (Springer, New York, 2013), Chap. 5.
- 43) T. Mizuno, R. Kanazawa, T. Aoki, and T. Sameshima, *Int. Conf. on Solid State Devices and Materials 2019: Extended Abstract of Solid State Devices and Materials, 2019* (Nagoya), (The Japan Society of Applied Physics), p. 887.
- 44) J. F. Ziegler, [<http://www.srim.org/>].
- 45) A. C. Ferrari and J. Robertson, *Phys. Rev. B* **64**, 075414 (2001).
- 46) C. Casiraghi, A. C. Ferrari, and J. Robertson, *Phys. Rev. B* **72**, 085401 (2005).
- 47) Rusli, J. Robertson, and G. A. J. Amaratunga, *J. Appl. Phys.* **80**, 2998 (1996).
- 48) S. J. Henley, J. D. Carey, and S. R. P. Silva, *Appl. Phys. Lett.* **85**, 6236 (2004).